Applied Surface Science 715 (2026) 164471

Contents lists available at ScienceDirect

Applied Surface Science

journal homepage: www.elsevier.com/locate/apsusc

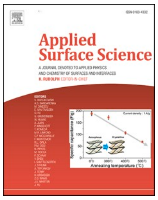

Full Length Article

Exploring the wear-resistant properties of three-dimensional “soft-ladder” shaped octa-aminophenyl polyhedral oligomeric silsesquioxane-crosslinked graphene oxide

Chang Tu [a], Rui Yuan [a,*], Lei Chen [b,*], Jing Yuan [c], Li Ji [b,*], Panpan Li [b], Bingxin Liu [a]

[a] *Salt Lake Chemical Engineering Research Complex, College of Chemical Engineering, Qinghai University, Xining 810016, China*
[b] *State Key Laboratory of Solid Lubrication, Lanzhou Institute of Chemical Physics, Chinese Academy of Sciences, Lanzhou, China*
[c] *Qinghai Provincial Key Laboratory of Nanomaterials and Technology, Qinghai Minzu University, Xining, Qinghai 810007, China*

ARTICLE INFO

Keywords:
Functionalized graphene oxide
Polyhedral oligomeric sesquisiloxanes
Wear resistance
“Soft ladder” structure

ABSTRACT

Designing the 3D structure of 2D nanomaterials is one of the effective measures to enhance their wear resistant. Here, we used graphene oxide (GO) as a template and selected mono-aminopropyllsobutyl polyhedral oligomeric silsesquioxane (MAPOSS) and octa-aminophenyl polyhedral oligomeric silsesquioxane (OAPOSS) to prepare a “plate-anchor” shaped MAPOSS-GO (2D) and three-dimensional cross-linked “soft ladder” shaped OAPOSS-GO (3D). From the friction experiments (0.5 N), the lubricant film formed by OAPOSS-GO (393 nm) is thicker and more regular than MAPOSS-GO (268 nm) and GO (70 nm). The wear life of OAPOSS-GO (289 min) is higher than that of MAPOSS-GO (174 min) and GO (49 min). Molecular dynamics simulations (MD) further revealed the reasons for the improved wear resistance of the OAPOSS-GO. Firstly, Polyhedral Oligomeric Silsesquioxane (POSS) improves GO-substrate binding and promotes a more regular arrangement of nanosheets. Secondly, the covalent bond between OAPOSS and GO resists the friction of the nanosheets during the sliding process, resulting in the formation of a thicker lubrication film; thirdly, the “soft ladder” structure facilitates the formation of physical occlusion without covalent bonding between different nanosheets, increasing the stability of the lubrication film. Therefore, our study provides a theoretical basis for the preparation of highly wear-resistant layered nanomaterials.

1. Introduction

Two-dimensional (2D) materials such as graphene are widely used in the field of lubrication due to its good chemical stability, high specific surface area, high in-plane strength and low interlayer shear strength [1,2]. Many groups have achieved lower friction coefficient and longer friction life of graphene by controlling the pressure [3], atmosphere [4], microstructure of the friction surface, temperature [5] and so on. [6,7] However, the conditions for graphene to achieve low lubrication are harsh, which requires not only a more regular structure but also special pre-treatment process (e.g. vacuum pre-friction, etc), making it difficult to be applied on a large scale. Therefore, achieving better wear-resistance performance of graphene-based coating through structural design [8] and functional modification [9] is one of the effective ways to promote their large-scale application. For example, F Mindivan et al investigating the effects of rosehip extract and other substances on the synthesis and application of graphene oxide [10–14].

Graphene oxide (GO), a product of graphene oxidation, has a large specific surface area, is well dispersed and contains oxygen-containing functional groups [15]. Oxidation treatment can effectively increase the combination of graphene and the substrate, enhance the van der Waals force between the nanosheets, and thus improve the wear resistance [16,17]. Although the wear resistance of GO is improved compared to graphene, the stability of its coatings in long-term applications is still poor, and thus further functional modification are required. In recent years, there has been a proliferation of representative studies on durable surface coatings derived from novel graphene oxides, which have provided valuable insights into this field [18–23]. Polyhedral oligomeric sesquisiloxanes (POSS) are cage structures consisting of alternating Si-O linkages. The diversity of reactive groups provides greater binding sites for the microstructure of POSS-based hybrid materials [24,25]. Nidhin Divakaran et al [26] improved the tensile

---

* Corresponding authors.
E-mail address: yuanruiqhdx@163.com (R. Yuan).

https://doi.org/10.1016/j.apsusc.2025.164471
Received 16 June 2025; Received in revised form 17 August 2025; Accepted 28 August 2025

strength, thermal decomposition temperature, and electrical conductivity of unsaturated polyesters through the combination of aminopropylisobutyl POSS with polypeptide bonding of graphene oxide. Liao et al [27] prepared octaaminophenylsiloxane functionalized GO reinforced polyimide composites with low dielectric constant and excellent mechanical properties. Sun et al [28] reduced the frictional wear of polyamide 6 by POSS functionalized GO. Bo Yu et al [29] improved friction and wear properties of base oils by POSS modification of GO. Our team designed and synthesized “plate-anchor” shaped POSS-GO nanosheets in our previous work and found that the interlocking structure formed by the “plate-anchor” structure during friction could also improve its wear-resistant [30,31]. However, previous studies were limited to the functional modification of single GO nanosheets at two-dimensional level, and there is a lack of research on the effect of the three-dimensional structure formed by connecting multiple GO nanosheets via POSS on the wear-resistant properties.

Based on this, our paper focuses on the three-dimensional structural construction of nanosheets, using octa-aminophenyl polyhedral oligomeric silsesquioxane (OAPOSS) to functionalize GO, and synthesizing cross-linked OAPOSS-GO with a “soft ladder” structure through the polyamino structure of OAPOSS. The effect of three-dimensional cross-linking on the friction and wear properties of GO is systematically investigated. Otherwise, molecular dynamics simulations were used to investigate in depth the microstructural evolution and tribological properties of OAPOSS-GO during the enrichment, loading and sliding. our work provides new ideas for designing GO molecular structures with excellent wear resistance.

2. Experimental

2.1. Materials

Graphene oxide (GO 99.5 %) powder was purchased from Nanjing JCNANO Technology Co., Ltd (Nanjing, China) Aminopropyllsobutyl POSS (OM-POSS 99.0 %) and N-Phenylaminopropyl POSS (OA-POSS 99.0 %) were purchased from Hybrid Plastic (Hattiesbury, Mississippi, USA). N-(3-Dimethylaminopropyi)-N’-ethylcarbodiimide hydrochloride (EDC 98 %) was purchased from Alladin Chemicals Ltd. (Shanghai, China). Ethanol(99.7 %) and Tetrahydrofuran(99.0 %) were provided by Maclean’s Biochemical Technology Co. (Shanghai, China) Monocrystalline silicon (99.0 %) was obtained from Kaihua LiJing Electronics Co Ltd (Quzhou China).

2.2. Synthesis of POSS functionalized-GO

GO powder (0.5 g), EDC (1.0 g), 2.0 g (MA-POSS/OA-POSS) were slowly added in the tetrahydrofuran (200 ml). The mixture was subsequently ultrasonicated for 1 h (40 kHz), then place in an oil bath with magnetic stirring at 50℃ for 48 h. After reaction finished, the resultant product was centrifugated (10,000 rpm for 5 min). The precipitate was successively washed with THF and ethanol three times. The product was dried in a vacuum oven at 50 ℃ for 12 h. The synthesis procedure is specified in Fig. 1a.

2.3. Preparation of GO-based coating

Before spraying, the wafers were sonicated in deionized water and ethanol for 5 min and then dried under nitrogen. MAPOSS-GO/OAPOSS-GO was added to 50 ml of ethanol at a mass concentration of 1 g L^{-1}. The dispersion was sprayed uniformly onto the silicon wafer under 0.2 MPa, dry, high purity nitrogen. The coating was vacuum dried at 80 °C for 1 h to remove residual solvent. (Coating thickness of approximately 1.3 μm) Materials and instruments were listed in supplementary data.

2.4. Characterization

The surface morphologies of nanocomposites and its frictional interfaces were observed by field emission scanning electron microscopy (FESEM, JSM-7900F, JEOL, Japan, 10 kV, secondary electron imaging), energy-dispersive X-ray spectroscopy (EDS, JSM-7900F, JEOL, Japan, 15 kV), transmission electron microscopy (TEM, Spectra 300 Thermo Fisher, USA, 200 kV, HAADF-STEM) and Optical 3D Surface Profiler (SuperView W1, CHOTEST, China). The thickness of the nanosheets were conducted by Atomic Force Microscope (AFM Dimension ICON, Bruker, USA, tapping mode in air, 25 ℃, distribute the ethanol solution containing the dissolved powder onto the silicon wafer.). The structure

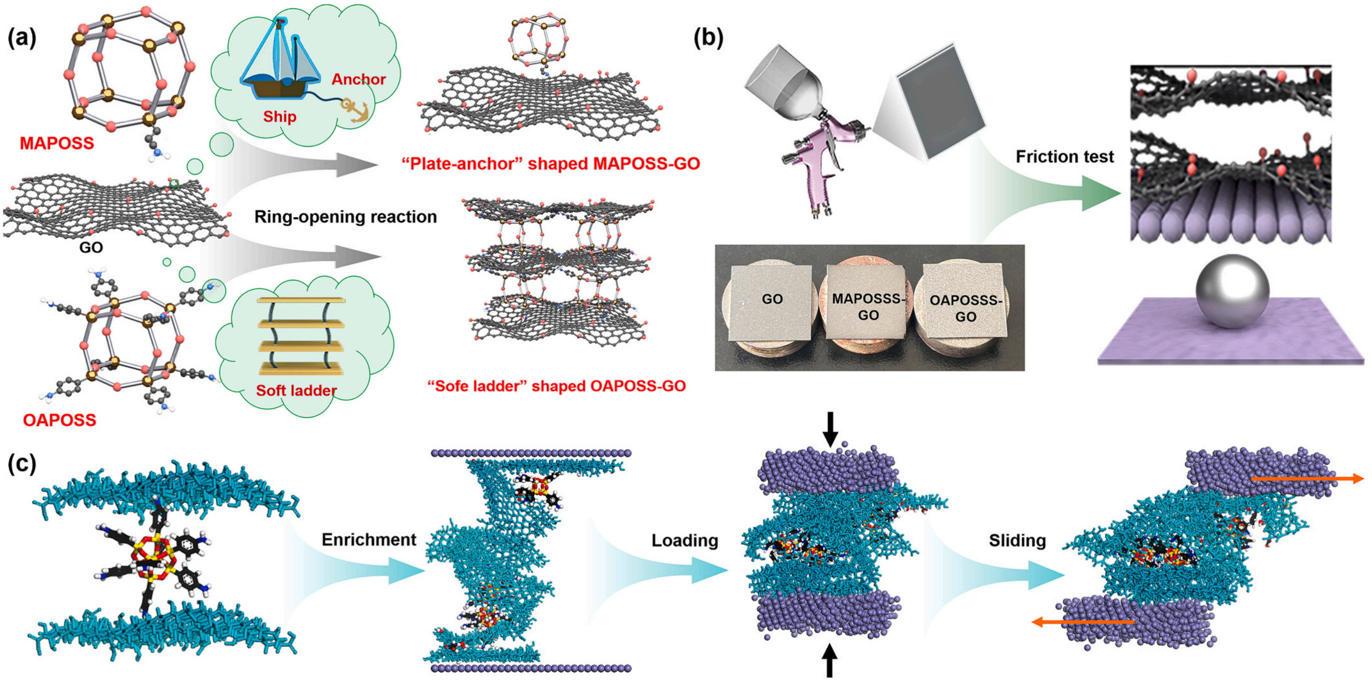

Fig. 1. (a) Synthesis process, (b) friction testing and (c) MD simulation process of GO-based coatings.

and chemistry properties of the samples were determined with an X-ray photoelectron spectroscope (XPS, ESCALAB, Thermo Fisher, USA, X-ray, C 1s at 284.8 eV, Shirley method, Gaussian-Lorentzian mix, 200 eV for survey scan, 20 eV for high-resolution scan), Fourier transform infrared spectrometry (FTIR, Nicolet 6700, Thermo Fisher, USA), X-ray diffraction (XRD, D-max2500PC, Rigaku, Japan, Cu target, powder pellet, 2D, Jade). GO internal defects were studied using Raman spectroscopy (InVia Qontor, Renishaw, UK, Renishaw inVia Raman microscope, 532 nm). Raman Mapping uses wire software to image the collected Raman signals as the ratio of the D peak and G peak. Contact angle analyzer (CA, OCA50, Dataphysics, Germany) and thermogravimetric analysis (TGA, STA449F3-DSC200F3, Netzsch, Germany, 800 ℃ under nitrogen atmospheres with a heating rate of 10 ℃/ min). Anton Paar STeP 500 Measuring coating bonding with nano-scratch (STeP 500, Anton Paar, Austria, Begin Load:1N, End Load:5N, length 3 mm, Rockwell).

2.5. Friction and wear test

The friction and wear tests were conducted using a ball-on-disc setup. The tribological properties of the coatings were investigated by means of a tribometer (MS-T3001 clhis China) at room temperature (25 ± 2℃), at a speed of 800 r/min (V = 420 mm/s), a radius of 5 mm, with a load of 0.1, 0.3, 0.5, 0.7 N on GCr15 steel balls (Stability of operating environment and friction behavior, Ø=6 mm, Ra = 20 nm) with at least three repetitions of each experiment. The friction test is specified in Fig. 1b.

2.6. Computational analysis

Molecular dynamics simulation with a full atomistic force field was conducted to study the tribological performances of GO, MAPOSS-GO and OAPOSS-GO [32–34]. The geometric optimization of the computational model and subsequent kinetic calculations were performed using the COMPASS (Condensed-phase Optimized Molecular Potentials for Atomistic Simulation Studies) force field [35]. The simulation temperature was implemented by Nóse-Hoover thermostat (excluding the direction of sliding from the temperature calculation) with a Q ratio of 0.01 [36]. The Atom based method and Ewald method were used to calculate the van der Waals and the long-range electrostatics of simulation [37].

The molecular structures of GO, MAPOSS-GO and OAPOSS-GO are depicted in Fig. S1. The GO was obtained from the oxidation of graphene and consisted of 300 carbon atoms. Based on the XPS results used in the experiments, GO were designed with carboxyl (9) and carbonyl (27) groups at the edges and epoxy (40) and hydroxyl (38) groups on the surfaces. By analyzing the synthesized products, the molar ratios of GO to POSS in MAPOSS-GO and OAPOSS-GO were close to 1:1 and 1:2, so that only one MAPOSS was grafted on the surface of each lamella in MAPOSS-GO, while two GO sheets were attached to each OAPOSS in OAPOSS-GO. Due to the limitations of the computing equipment, the number of the GO flakes added to each system was controlled to be 6. To further investigate the friction process, the Fe (−1 0 0) metal surface was selected as the upper and lower friction interfaces, and the corresponding vacuum layer was established. Expansion of the established Fe layer to be mutually consistent with the initial GO, MAPOSS-GO and OAPOSS-GO systems. Build GO-based systems as a middle layer and add Fe layers above and below it and label as top-wall and bottom-wall [38]. Periodic boundary conditions were used along three directions, while vacuum space was intentionally reserved at the top and bottom along the pressure direction [39].

All initial structures were first geometrically optimized using the Smart algorithm. And then the NVT (constant number of particles, volume and temperature) [40] dynamic equilibration was then performed in 3 steps: (1) 1 ns of NVT simulation at 0.25 fs time step to study the slow enrichment of GO-based flakes on the Fe surface; (2) 5 ns of NVT simulation at 0.5 fs time step for the system to reach dynamic equilibrium; (3) An additional 1 ns for data collected at 1000 steps intervals to get mean square displacement (MSD) [41], radial distribution function (RDF) [42] and so on. For the friction process, an additional NPT (constant number of particles, pressure and temperature) [43–45] dynamics equilibration was running for 1 ns with time step 0.25 fs and the corresponding pressures were 0.223 GPa, 0.091 and 0.084 GPa, based on the actual experimental contact area and load (Fig. S2). The above systems were then subjected to NVT simulation for 1 ns, followed by confined shear with velocity of 0.04 m/s (1 ns, 0.2 fs).

To better illustrate the structural changes of the coatings from preparation to friction testing, the MD simulations are divided into three parts: enrichment, loading and sliding, as shown in Fig. 1c.

3. Results and discussion

3.1. Characterization of the GO, MAPOSS-GO and OAPOSS-GO

The morphologies of GO, MAPOSS-GO and OAPOSS-GO are shown in Fig. 2. The FESEM image of GO shows a typical flat but slightly wrinkled surface (Fig. 2a). After functional modification, the surface folds of MAPOSS-GO and OAPOSS-GO become more wrinkled (Fig. 2b-c). EDS mapping results show that MAPOSS and OAPOSS are uniformly distributed on GO. Similarly, the present of POSS microspheres in MAPOSS-GO and OAPOSS-GO are observed in the TEM images (Fig. 2d-f, red circles). The SAED patterns of GO and OAPOSS-GO show a typical ring like pattern showing a polycrystalline structure, the SAED pattern of OAPOSS-GO shows typical hexagonal structure. Meanwhile, the introduction of POSS on GO increases its crystal spacing from 0.40 nm (GO) to 0.79 nm (MAPOSS-GO) and 1.13 nm (OAPOSS-GO), indicating that MAPOSS-GO and OAPOSS-GO are looser and easier to exfoliation than GO.

As shown in Fig. 3a-c, GO and MAPOSS-GO show a monolayer distribution with thickness of about 1.68 nm and 3.45 nm. The three-dimensional stacking structure of OAPOSS-GO is very obvious with a thickness of about 4.53 nm.

The “soft ladder” structure of OAPOSS-GO was further investigated. As shown in Fig. 4a, the surface of GO flakes was clearly enriched with OAPOSS aggregates with crystal plane spacing of about 0.25 nm. What was more noteworthy is that GO has more raised portions on the surface. Electron diffraction studies revealed that this raised portion contains not only the characteristic peaks of GO but also those of OAPOSS, indicating that OAPOSS is sandwiched between the two GO layers, which links adjacent GO layers together, forming a “soft ladder” structure. Similarly, OAPOSS-GO forms a distinct laminar structure in the SEM images (Fig. 4b). Furthermore, the three-dimensional stacking structure of OAPOSS-GO is very obvious in AFM images (Fig. 4c). The number of layers is concentrated at 3–4. This layered distribution not only indicates the orderly stacking of the layers, but also provides deep insights into the stability and uniformity of the overall three-dimensional “soft ladder” structure. Wear trajectory.

The structures and chemical properties of GO-based nanocomposites are investigated by XPS, FTIR, Raman, XRD and TG. As shown in Fig. 5a, the additional peaks around 100 eV (Si 2p), 150 eV (Si 2 s) and 400 eV (N 1s) appear in MAPOSS-GO and OAPOSS-GO, indicating that the POSS is successfully introduced onto GO nanosheets. The results of the deconvolution process for the C 1s and N 1s high-resolution spectra are shown in Fig. 5b-f. The N 1s spectra are deconvoluted into Gaussian peaks around at 399.6 eV, 401.4 eV and 402.0 eV, corresponding to neutral N-C, N-C(O) and NH_3^+-C groups [46]. MAPOSS-GO and OAPOSS-GO appear with 26.0 % and 11.5 % N-C(O) characterization groups. Compared with GO, the C1s XPS spectra of MAPOSS-GO and OAPOSS-GO show an additional C-N peak at 287.2 eV and a significant decrease in the C-O-C peak, which indicate that the $–NH_2$ group in POSS mainly react with the C-O-C group in GO. Similarly, the ring-opening reaction between GO with MAPOSS and OAPOSS is also confirmed by FT-IR analysis (Fig. 5g). The strong absorption band at around 1108

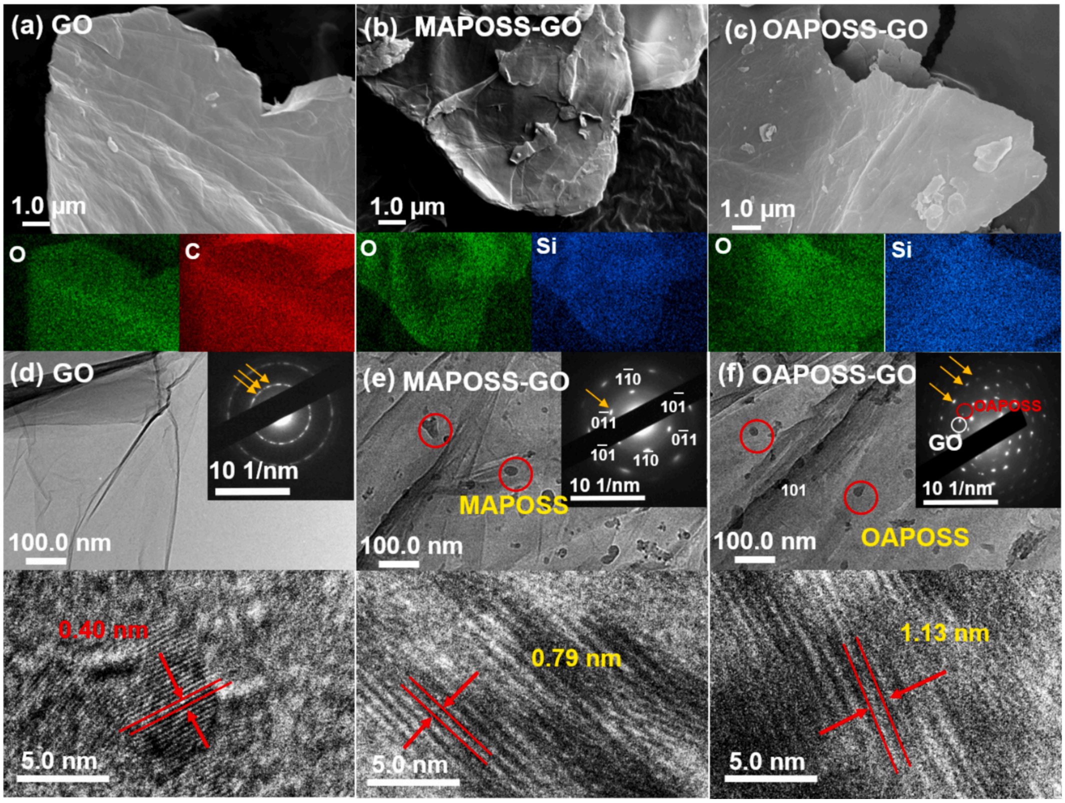

Fig. 2. GO, MAPOSS-GO and OAPOSS-GO (a-c) FESEM images and the corresponding EDS maps; (d-f) TEM images and the corresponding SAED.

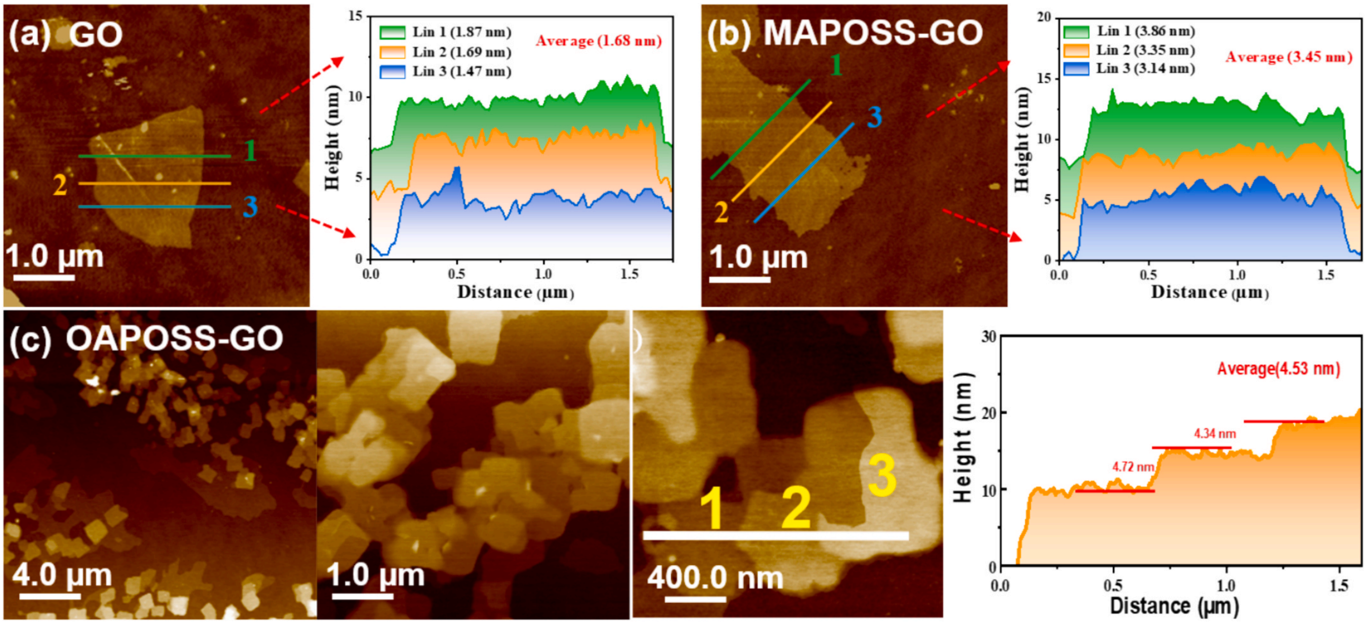

Fig. 3. GO, MAPOSS-GO and OAPOSS-GO (a-c) AFM images and its thickness distribution.

cm^{-1} is attributed to the Si-O-Si group in POSS, and the peak at 1650 cm^{-1} is corresponding to the stretching vibrations of the –NH groups [47].

Raman spectroscopy can be used to analyze structural changes in graphene oxide. As shown in Fig. 5h, the Raman spectra of graphene oxide-based materials all exhibit two distinct peaks at 1350 cm-1 and 1590 cm-1, corresponding to the D peak and G peak, respectively. The D peak represents lattice defects in carbon atoms, while the G peak represents plane-inner stretching vibrations of sp-hybridized carbon atoms. Typically, the intensity ratio of the D peak to the G peak is used to assess the orderliness and integrity of the material's structure. When GO is functionalized with POSS, the functional groups on POSS form chemical bonds with graphene oxide, disrupting the original graphene oxide structure and leading to an increase in internal defects. the I_D/I_G ratios of MAPOSS-GO (0.90) and OAPOSS-GO (0.93) are higher than those of GO (0.80). This is due to the structural deformation caused by

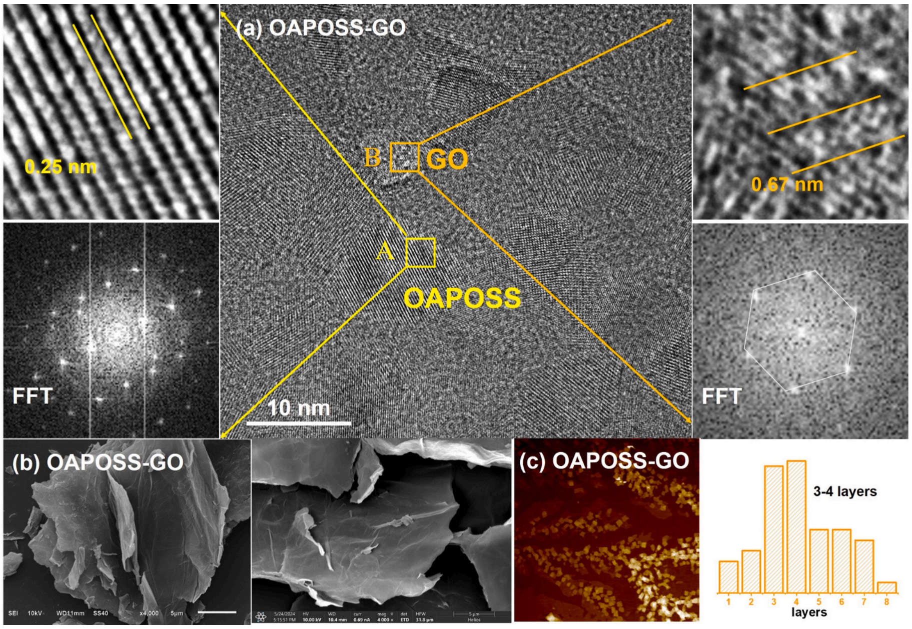

Fig. 4. Characterization of the "Soft ladder" structure of OAPOSS-GO (a) TEM images and the corresponding SAED; (b) SEM images; (c) AFM images and its layer distribution.

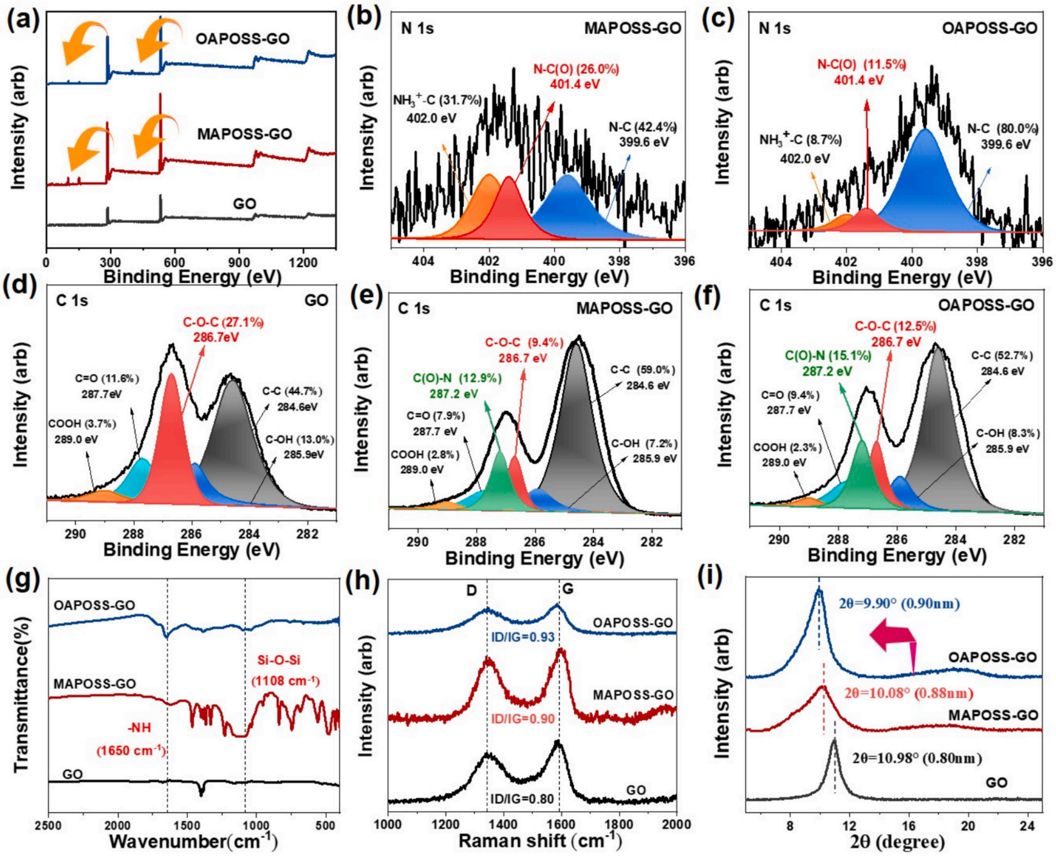

Fig. 5. Structure characterization of GO, MAPOSS-GO and OAPOSS-GO coating. (a-f) XPS survey and high-resolution spectra of N 1s and C 1s; (g-i) FTIR, Raman and XRD patterns.

the grafted bulk POSS [48]. Similar results are shown in Fig. 5i, the layer spacing of GO, MAPOSS-GO and OAPOSS-GO increases from 0.80 nm (10.98° 2θ) to 0.88 nm (10.08° 2θ) and 0.90 nm (9.90° 2θ), which further confirms that the introduction of POSS enlarged the layer spacing of GO and prevents the nanosheets from restacking [49]. In addition, grafting POSS also improves the thermal stability of GO (Fig. S3).

3.2. Friction and wear properties of GO, MAPOSS-GO, OAPOSS-GO coating

The distribution of GO, MAPOSS-GO, OAPOSS-GO coatings are shown in Fig. 5a-c. The functional groups in OAPOSS and MAPOSS effectively inhibit the stacking of layers during the coating preparation process through bridging graphene oxide flakes, thereby forming thicker coatings. GO and MAPOSS-GO coatings show folded nanosheets with surface roughness of 0.646 μm and 0.377 μm. In contrast, the roughness of OAPOSS-GO coating is only 0.158 μm, and the coating surface is very regular with flakes almost closely aligned in parallel, which indicates that OAPOSS-GO has better affinity with the substrate. To confirm the simulation results, we performed a nano-scratch experiments and shown in Fig. 6g-h. The OAPOSS-GO coating has the smallest acoustic emission amplitude. Signals with smaller amplitudes usually indicate less material deformation, which suggests the strongest bonding between OAPOSS-GO and the substrate. Therefore, the introduction of POSS can enhance the adhesion of GO to the substrate. Meanwhile, the introduction of POSS also increases the hydrophobicity of the coatings (Fig. S4), with water contact angles of 61.46° (GO), 105.38° (MAPOSS-GO) and 98.15° (OAPOSS-GO) [50]. This is mainly attributed to the fact that the nanocage structure of POSS forms micro- and nano-rough structures on the coating surface, which traps air and forms a "solid-air composite interface". Meanwhile, the low surface energy nonpolar groups on the surface of POSS reduce the intrinsic surface energy of the coating. According to the Wenzel model [51] Cos theta r = r Cos theta s, roughening can further amplify this hydrophobic property, and these two effects synergistically enhance the hydrophobicity.

To confirm the influence of the "soft-ladder" structural assembly on the wear-resistant properties, the coefficient of friction and service life of GO, MAPOSS-GO and OAPOSS-GO coatings are investigated. As shown in Fig. 7a-h, none of the three coatings are worn through at a load of 0.1 N (2 h). With the increase of load, the wear resistance of GO coating decreases significantly with the service life of 83 min (0.3 N), 49 min (0.5 N) and 34 min (0.7 N). Compared with GO, the "plate-anchor" shaped MAPOSS-GO has better wear resistance and only wears through under a load of 0.7 N (71 min). It is worth noting that "soft ladder" shaped OAPOSS-GO coating did not wear through during the friction (2 h). The service life of the GO, MAPOSSS-GO and OAPOSS-GO coatings are further conducted to be 49 min, 174 min and 289 min at 0.5 N load (Fig. S5). These mean that the OAPOSS-GO coating has the best wear resistance, confirming the feasibility of improving the wear resistance of GO by assembling a 3D "soft ladder" structure. In addition, the roughness of coatings affects the coefficient of friction (COF) during the run-in period [52], as shown in Fig. 5h-k, the GO coating with the largest roughness has the highest COF during the run-in period.

To quantify the source of the excellent wear resistant performance of the OAPOSS-GO, the lubricant films of the three coatings are investigated at 0.1 N (all unworn) and 0.5 N (partially unworn).

0.1 N:Under 0.1 N load (Fig. 8a-f), GO, MAPOSS-GO and OAPOSS-GO can form a relatively continuous Lubricant film, but their Lubricant film sizes varied greatly. For GO, the Lubricant film is narrower and thinner, with a width and height of 10 μm and 300 nm. The MAPOSS-GO formed a lager Lubricant film than GO (width and height of 50 μm and 400 nm). In comparison, OAPOSS-GO coating has the largest and thickest Lubricant film, with a width and height of 110 μm and 500 nm. However, a dense and thick lubricant film effectively increases the contact area between the coating and the steel ball, thereby increasing the coating's service life.

Furthermore, Raman spectroscopy is used to investigate the defects in the Lubricant film formed by the GO-based nanosheets during friction. As shown in Fig. 9. Raman mapping and I_D/I_G values of the contact region of GO, MAPOSS-GO and OAPOSS-GO coatings (ball-on-disk tribometer, 0.1 N), with different colors in the Raman mapping representing different I_D/I_G values. The defect density at the center of the wear marks increases significantly. During friction, the center of the

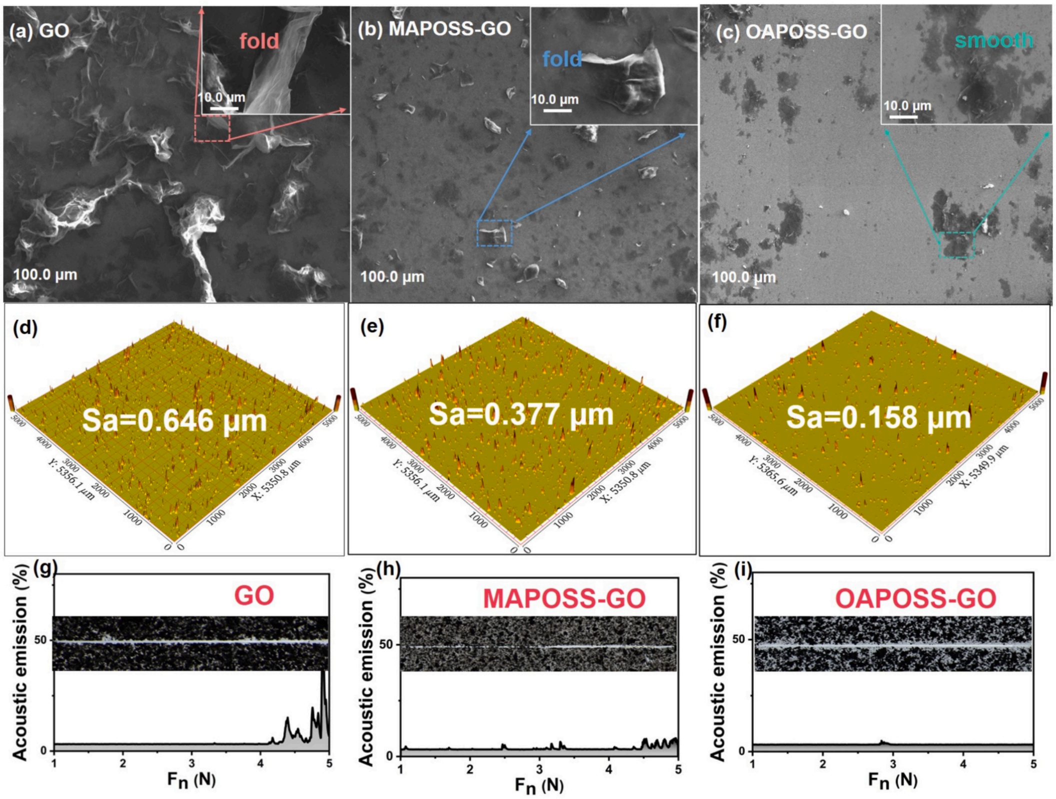

Fig. 6. Morphology and frictional performances of GO, MAPOSS-GO, OAPOSS-GO coating. (a-c) SEM (250x and 2000x) images, (d-f) 3D topographies; (g-i) Nano-scratch of the GO, MAPOSS-GO and OAPOSS-GO coatings.

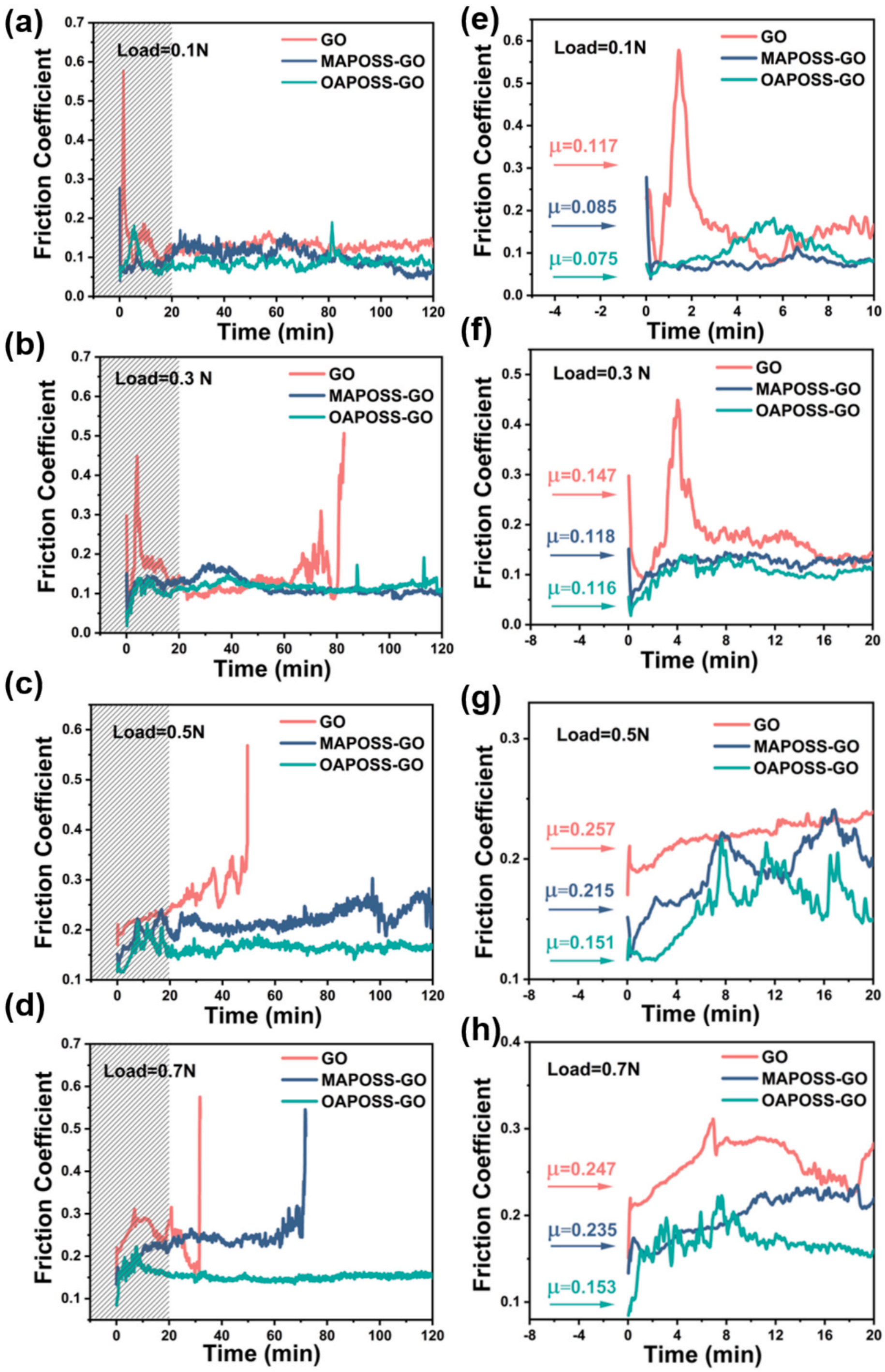

Fig. 7. GO, MAPOSS-GO, OAPOSS-GO coating. (a-h) Coefficient of friction as a function of sliding time (120 min) under various loads (0.1 N, 0.3 N, 0.5 N,0.7 N).

wear marks is subjected to maximum normal stress and shear stress, causing the van der Waals forces between GO layers to be disrupted, resulting in a large number of edge defects and lattice distortions in the carbon skeleton. In addition, intense friction may be accompanied by local high temperatures, but GO has poor thermal stability, and high temperatures can easily trigger amorphous transformation, further exacerbating structural disorder and increasing the I_D/I_G ratio. It is worth noting that higher I_D/I_G values mean that some carbon atoms of GO on the six-membered rings form sp^3 hybrid bonds with oxygen after oxidation [53]. This destroys the ideal six-membered ring carbon structure and increases the degree of disorder. As shown in Fig. 9a-c, the GO coating is light red and has an I_D/I_G value around 1.18, and the MAPOSS-GO and OAPOSS-GO coatings are light green with an I_D/I_G value of 1.03 and 1.08. This means that the introduction of POSS on GO nanosheets can effectively reduce its defect during friction. The reduction of defects may be related to the following two factors: firstly, the height and the size of the lubricant film of MAPOSS-GO and OAPOSS-GO are larger, which results in a reduction of the pressure distributed to each nanosheet; secondly, the larger size of POSS acts as a cushion during the friction, which in turn serves to protect the nanosheet. In addition, the Lubricant film of both GO and MAPOSS-GO show a characteristic peak signal of 520 cm^{-1} (Si, substrate), while that of OAPOSS-GO is not obvious, further indicating that the Lubricant film of OAPOSS-GO is dense and thick.

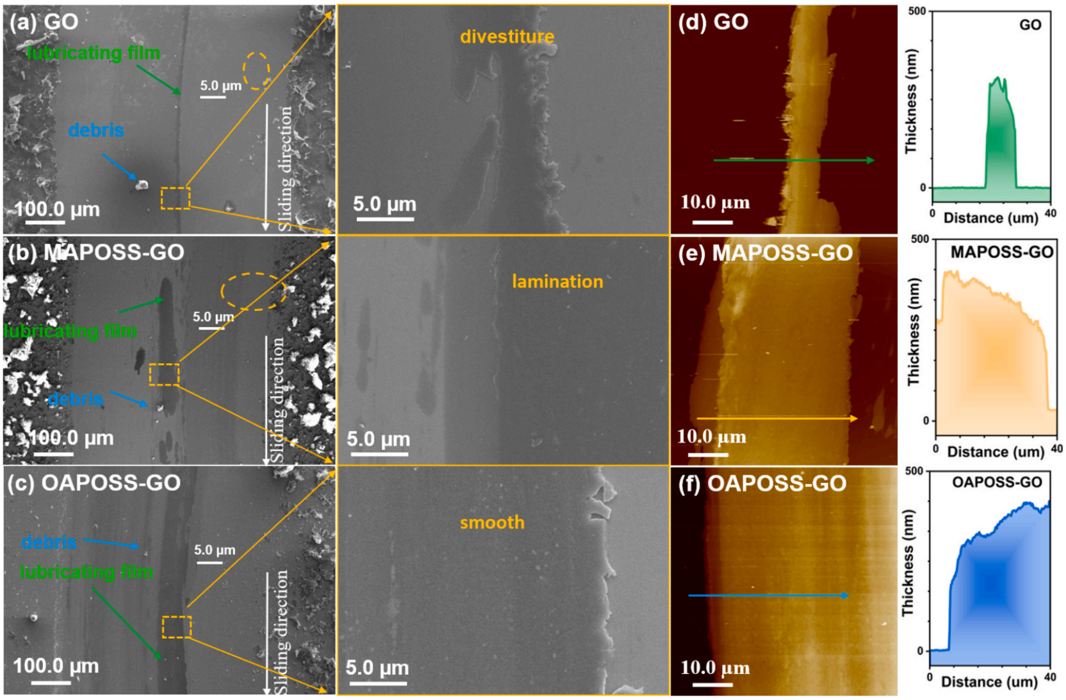

Fig. 8. Structure characterization of the wear track of GO, MAPOSS-GO and OAPOSS-GO coatings at 0.1 N load. (a-c) SEM and (d-f) AFM images.

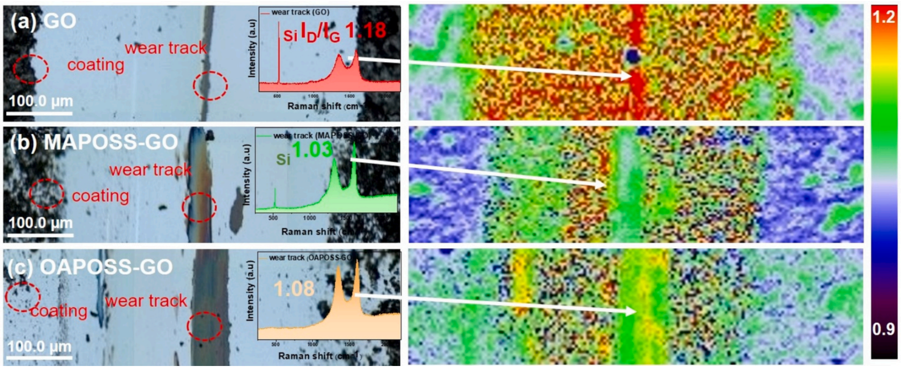

Fig. 9. Structure characterization of the wear track of GO, MAPOSS-GO and OAPOSS-GO coatings at 0.1 N load. (a-c) Raman mapping of I_D/I_G and the corresponding curves.

To further investigate the state of POSS enrichment at the contact surface, XPS etching of the lubricant film of OAPOS + S-GO is conducted and shown in Fig. 10a-c (depth profile, spot size 50 μm, etch cycle 30 s, cluster size 75, ion energy 6000 eV). The C 1s, O 1s, N 1s and Si 2p high-resolution spectra are deconvoluted. The peak intensity of C atom increases with etching depth, while the peak intensities of O, Si and N contained in POSS all decrease to some extent. This phenomenon indicates that POSS is significantly enriched on the surface of the Lubricant film and plays a role in the improvement of wear resistance.

0.5 N: Under 0.5 N load, as shown in Fig. S6, OAPOSS-GO has the largest wear point area, followed by MAPOSS-GO and GO. This further means that even though the same load is applied, the pressure force on the flakes is different because of the different contact areas. Based on the wear point area, the pressures on the contact surface of the GO, MAPOSS-GO and OAPOSS-GO coatings are calculated to be 0.223 GPa, 0.091 and 0.084 GPa. the height of GO, MAPOSS and OAPOSS balls are 33 μm, 36 μm and 43 μm, which confirms the difference in ball wear. Similar results are obtained in the wear track studies, as shown in

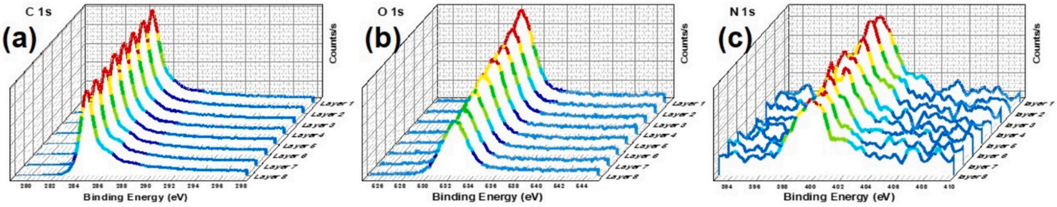

Fig. 10. Structure characterization of the wear track of OAPOSS-GO coatings at 0.1 N load. (a-c) XPS etching of OAPOSS-GO.

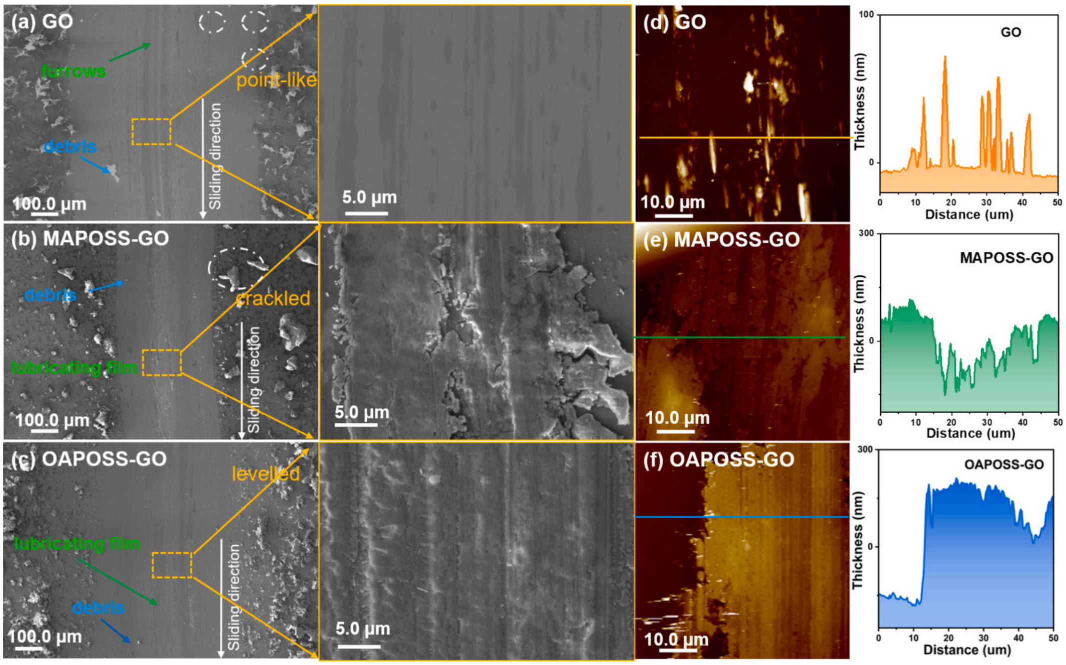

Fig. 11. Structure characterization of the wear track of GO, MAPOSS-GO and OAPOSS-GO coatings at 0.5 N load. (a-c) SEM and (d-f) AFM images of wear track;

Fig. 11a-f, where the GO coating has almost no continuous Lubricant film and the wear track show only a small spots, grooves and large particles of debris, with spot height ranging from 10-70 nm. The MAPOSS-GO has a Lubricant film with large holes and cracks, some debris in the wear track but no grooves. Its lubricant film is unevenly distributed with a height of 268 nm. In comparison, the Lubricant film of OAPOSS-GO coating is flat and dense with a height of 393 nm.

Fig. 12a-c shows the Raman mapping and I_D/I_G values of the contact areas of the GO, MAPOSS-GO, and OAPOSS-GO coatings. Compared to the 0.1 N load, the I_D/I_G ratio sharply increases under the 0.5 N load, characteristic peaks of the substrate material appear, and there is a significant difference in the I_D/I_G ratio between the undamaged area and the edge of the wear mark, Defect boundaries are clearly defined, with more severe defects in the coating, and the color is predominantly bright red. This indicates that higher loads and longer friction times lead to complete fragmentation of GO layers, disordered carbon frameworks, and the removal of a large number of oxygen-containing functional groups, resulting in increased defects in the nanosheets. The increase in defects reduces the bonding strength between nanosheets, causing them to peel off as wear debris and thereby reducing the height of the lubricating film. However, the superior wear resistance of the “soft trapezoidal” structure OAPOSS-GO coating is primarily attributed to the formation of a large, thick lubrication film during friction. The specific mechanism of action was further investigated through molecular dynamics simulations.

3.3. Microscopic wear resistance of GO, MAPOSS-GO and OAPOSS-GO

Film spraying process. As shown in Fig. 13a-c, at the initial stage (t = 0 ps), GO, MAPOSS-GO and OAPOSS-GO are uniformly distributed in the systems. As the simulation progresses, the nanosheets move closer to the Fe surface and form a stable enrichment, indicating that GO, MAPOSS-GO and OAPOSS-GO all have good affinity with Fe surface. The nanosheets enriched on the surface of the equilibrated Fe substrate are further labeled as layer 1, layer 2, layer 3 and layer 4. The distances of the nanosheets closest to the Fe surfaces of GO, MAPOSS-GO and OAPOSS-GO are 4.11 Å, 3.73 Å and 4.09 Å, suggesting that the grafting of POSS induces the nanosheets to be closer to the substrate. Compare with GO and MAPOSS, OAPOSS can form a more regular structure, due to its “soft-ladder” structure. The simulated trajectories of MAPOSS-GO and OAPOSS-GO also yielded the result that POSS favors the enhancement of the interfacial bonding of GO (Fig. 13d and Fig. S7). It is clear that MAPOSS first touches the Fe surface and then pulls the GO flat on the substrate. Magnifying the contact surface (100 ps) reveals that the

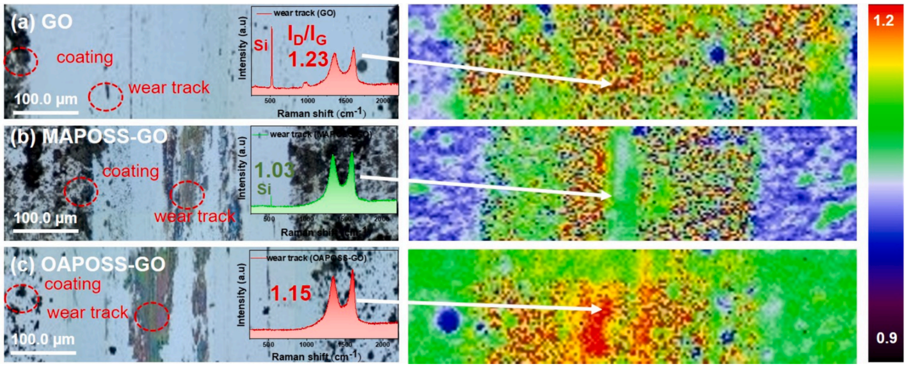

Fig. 12. Structure characterization of the wear track of GO, MAPOSS-GO and OAPOSS-GO coatings at 0.5 N load. (a-c) Raman mapping of I_D/I_G and the corresponding curves.

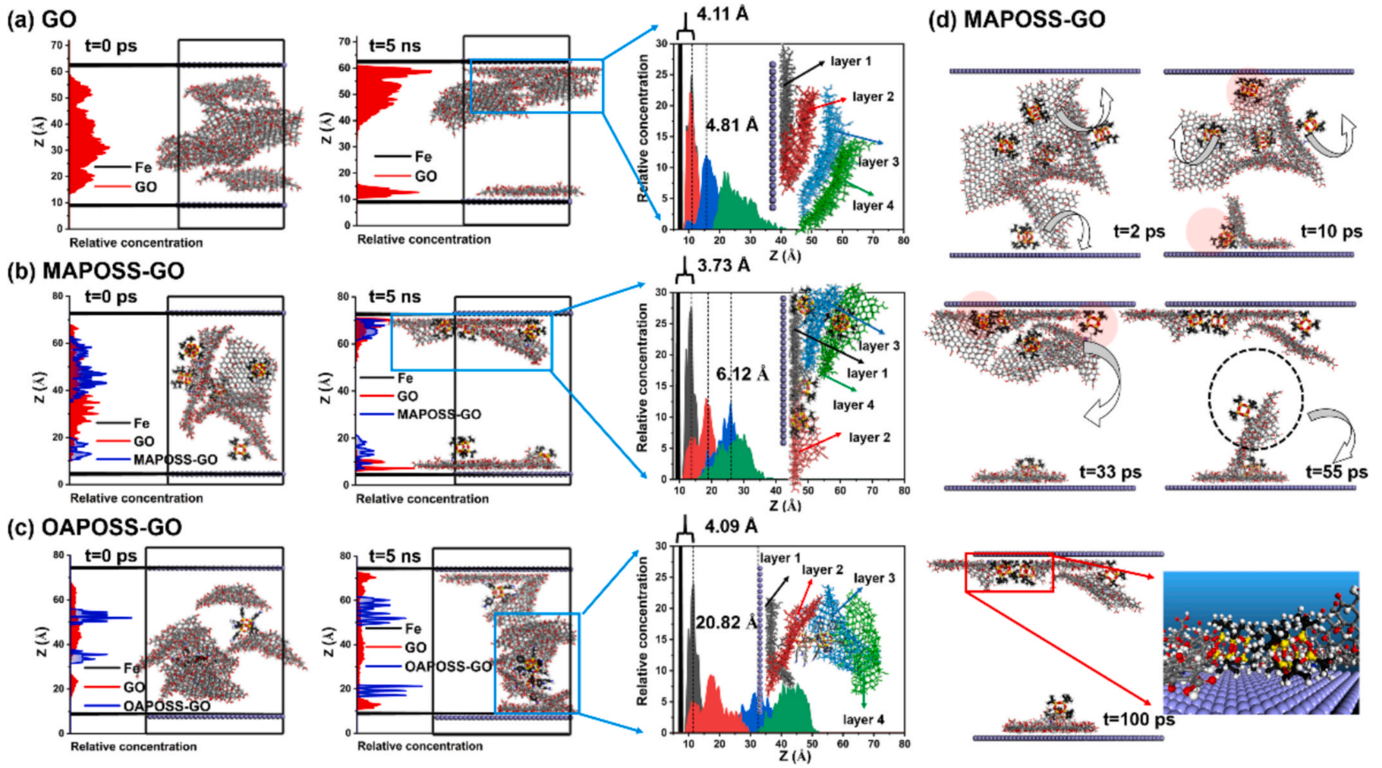

Fig. 13. (a-c) Snapshots of initial and equilibrated system and relative concentration of different layers in various coatings (C, light gray; O, red; Si, yellow; N, blue). (d) Snapshots of the MAPOSS-GO system at 2 ps, 10 ps, 33 ps, 55 ps and 100 ps (C (MAPOSS), black).

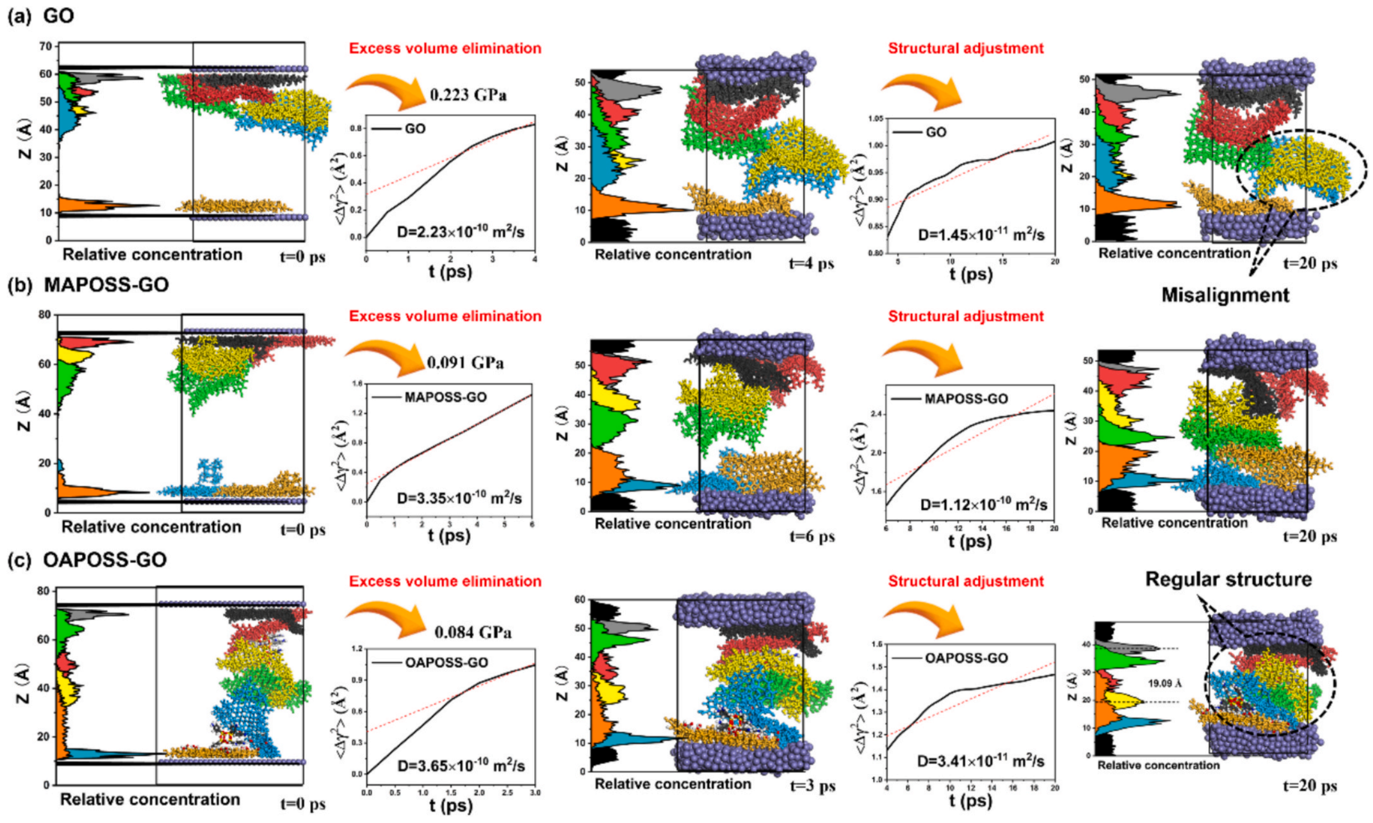

Fig. 14. Snapshot, relative concentration and MSDs of GO, MAPOSS-GO and OAPOSS-GO in the excess volume elimination step and structural adjustment step.

POSS is in direct contact with the Fe surface, further suggesting a good affinity between MAPOSS and substrate. However, there are two main roles of OAPOSS in the spraying process: firstly, OAPOSS enhances the bonding of GO to the substrate; secondly, the formation of “soft ladder” structure is conductive to the formation of more regular layers.

Load down process. Based on the contact area of coatings under a load of 0.5N in the friction experiment, the pressures of the GO, MAPOSS-GO and OAPOSS-GO are set to be 0.223 GPa, 0.091 GPa and 0.084 GPa. The dimensions of the simulated systems in the Z-axis direction decrease rapidly under load and remain essentially unchanged after 20 ps (Fig. S8). They may undergo two steps, as shown in Fig. 14, first, the excess space between the nanosheets is compressed and the layers gradually come into contact with each other (remarked as excess volume elimination), as reflected in a faster reduction in the cell length (labelled in red, within 4 ps). The simulation time required for the first step of GO, MAPOSS-GO and OAPOSS-GO are 4,6 and 3 ps. With the elimination of excess space, the arrangement between the nanosheets become more regular, and the layers move very fast at this stage. From 4 ps to 20 ps, the nanoflakes begin to adjust their structure (structural adjustment step) and eventually reach equilibrium under a combination of van der Waals repulsion and load pressure (Fig. S8). The motion of the nanoflakes also slow down significantly. The equilibrated OAPOSS-GO system has a more regular structure compared to GO and MAPOSS-GO, with a layer spacing of 19.09 Å, which is slightly smaller than that of the unpressurised layer spacing (20.82 Å).

Sliding process. The above equilibrium pressurized systems are subjected to confined shear with a Fe surface velocity of 4×10^{-4} m/s. The structural evolution of the MAPOSS-GO at 0 ps, 600 ps and 694 ps are shown in Fig. 15a. It is found that the MAPOSS-GO is dislocated under confined shear, where the bottom Fe, layer 1 and layer 2 form a stable structure, while the top Fe, layer 4, layer 5 and layer 6 form another structure, with layer 3 between them. Further statistics on the MSDs of layers and Fe in these structures. As shown in Fig. 15b-d, the MSD curves of bottom Fe, layer 1, layer 2 are very similar, and their corresponding diffusion coefficients are 2.03×10^{-9} m^2/s, 1.91×10^{-9} m^2/s, 1.64×10^{-9} m^2/s. In addition, the position of layer 1 and layer 2 on the bottom Fe is basically unchanged between the initial and the end of the simulation. This indicates that layer 1 and layer 2 form a stable lubricant film on the bottom Fe, labelled as lubricating film-B. Similarly, layer 4, layer 5 and layer 6 form another lubricant film on the top Fe, and the corresponding diffusion coefficients are 2.03×10^{-9} m^2/s, 1.51×10^{-9} m^2/s, 1.66×10^{-9} m^2/s and 7.57×10^{-10} m^2/s, remarked as lubricating film-T. While, layer 3 has a different trend from the other layers and substrates, which is the abrasive debris produced by friction. Its slip interface appears between the nanosheets, suggesting that the bonding between the MAPOSS-GO is not strong. Similar to the MAPOSS-GO, the GO also showed significant lamellar slip and abrasive debris during slip (Fig. S9).

Unlike GO and MAPOSS-GO, OAPOSS-GO is not dislocated during friction, and its final fracture is between layer 6 and the top Fe, so all nanosheets are retained as a whole on the bottom Fe (Fig. 15e). And all the nanosheets have the same motion trend during the sliding process. This strong interaction between the “soft ladder” shaped nanosheets may be responsible for the formation of large and thick lubricant films in OAPOSS-GO coating. Based on this, the main reasons for the excellent wear resistance of OAPOSS-GO coatings can be summarized as follows (Fig. 16). (1) The better bonding of OAPOSS-GO with the Fe surface. (2) OAPOSS-GO forms a thicker and denser lubricant film on the Fe surface.

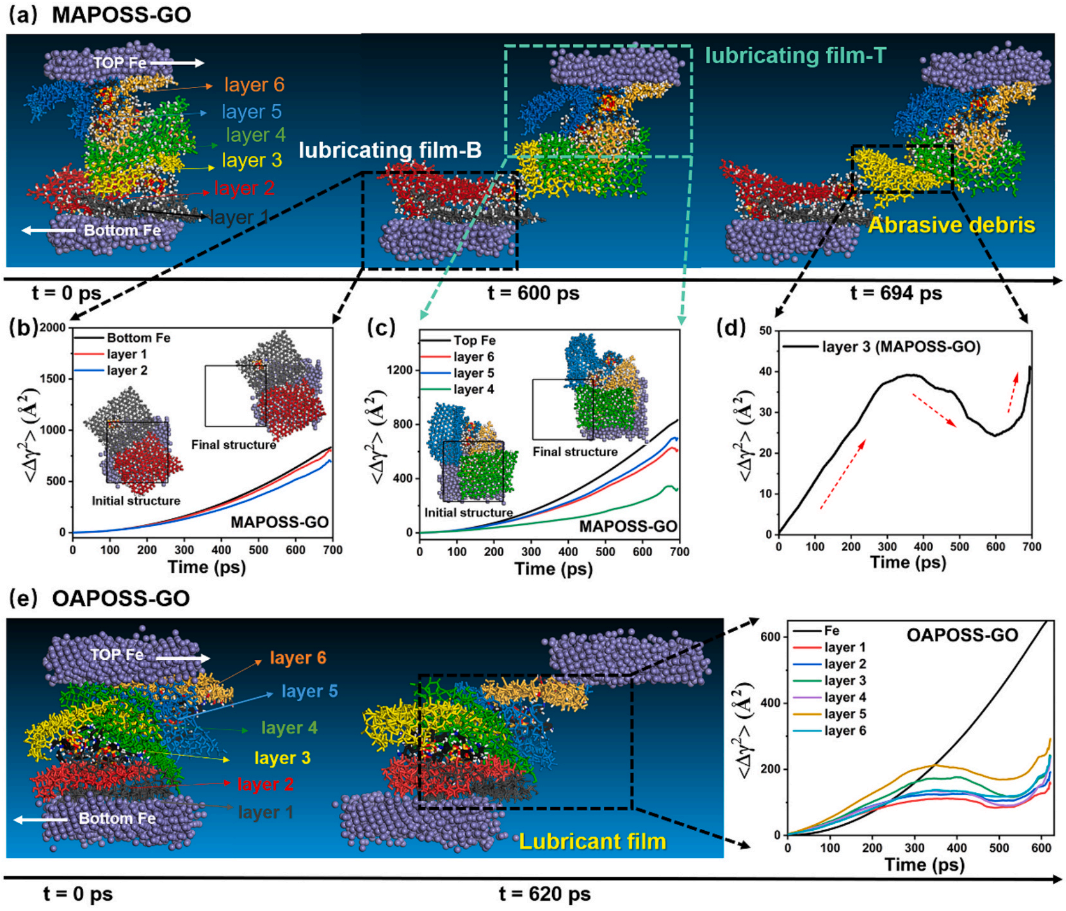

Fig. 15. (a) Snapshots of MAPOSS-GO at 0 ps, 600 ps and 694 ps. (b-d) MSDs of Fe substrate and nanolayers of MAPOSS-GO. (e) Snapshots of OAPOSS-GO at 0 ps and 620 ps and MSDs of Fe substrate and nanosheets.

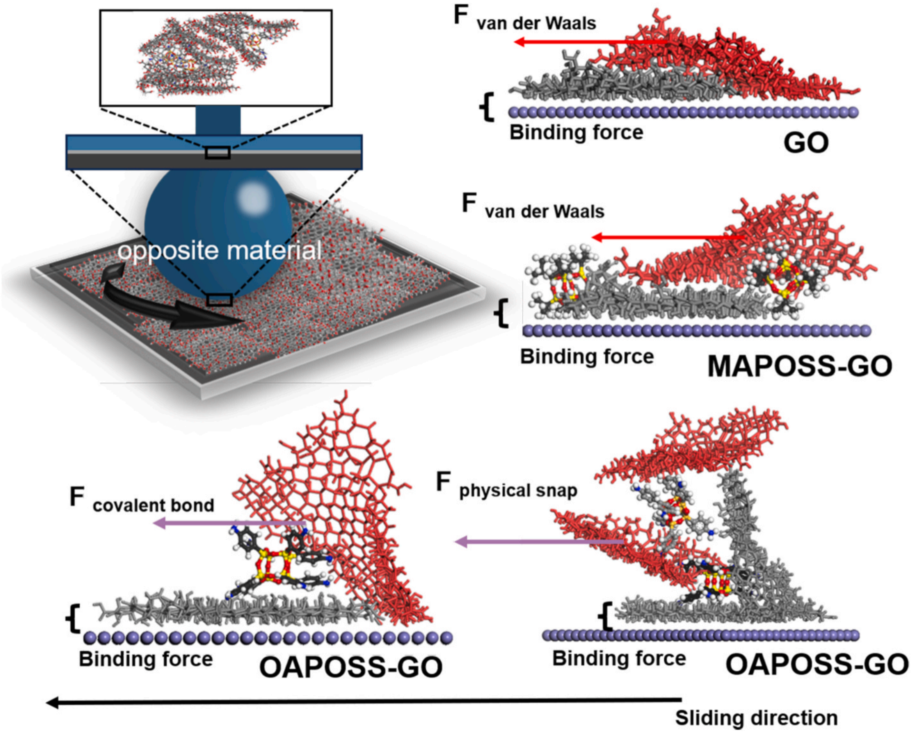

Fig. 16. Schematic of the interaction forces between GO, MAPOSS-GO and OAPOSS-GO nanosheets.

The construction of the "soft ladder" structure not only introduces stronger covalent bonds between the nanolayers, but also relies on the dislocations between the different nanolayers to form physical junctions, ultimately resulting in the formation of a very dense lubricant film during the friction process.

Of course, the strong interaction between the nanosheets leads to an increase in the coefficient of friction, which is detrimental to the lubrication properties. However, a prerequisite for the coating to maintain a low coefficient of friction for a long period of time is a good wear resistance. Otherwise, the broken interfaces also lead to a significant increase in the coefficient of friction, which explains the lowest coefficient of friction of the 3D crosslinked OAPOSS-GO in the macroscopic experiments.

4. Conclusion

In summary, "plate-anchor" shaped MAPOSS-GO and "soft ladder" shaped OAPOSS-GO are synthesized by the ring-opening reaction of epoxy on the surface of GO sheets. Among them, OAPOSS contains 8 amino groups which can act as ladder ropes to covalently bond the different nanosheet to form a "soft ladder" structure, while MAPOSS has only one amino group, which can be considered as an anchor when grafted on the GO surface, thus forming a "plate-anchor" structure. For further investigate the advantages of structured assembly of flakes, their tribological properties are determined. It is found that the wear life of OAPOSS-GO reaches 289 min, which is 5.2 times that of pure GO (49 min) and 1.7 times that of MAPOSS-GO (174 min). This significant improvement is attributed to the lubricating film formed on the worn surface of OAPOSS-GO, which has a height of 393 nm, 1.7 times that of the film formed by MAPOSS-GO (268 nm) and 5.6 times that of the film formed by pure GO (70 nm). The microscopic tribological properties of GO, MAPOSS-GO and OAPOSS-GO are also investigated using MD simulations. During the film spraying process, the grafting of POSS promotes the formation of a more stable bond between GO and the substrate while reducing the coating roughness. In the load-down stage, OAPOSS tightly connects different nanosheets through covalent bonding, which results in a tighter arrangement of the GO layer under load and less prone to large dislocations. In subsequent friction, OAPOSS-GO is able to rely on covalent bonding and physical snap effects between the nanolayers to stabilize itself at the interface and eventually form a thicker lubricant film.

CRediT authorship contribution statement

Chang Tu: Writing – original draft, Resources, Methodology. **Rui Yuan:** Writing – review & editing, Investigation, Funding acquisition, Conceptualization. **Lei Chen:** Software, Methodology. **Jing Yuan:** Methodology, Data curation. **Li Ji:** Resources, Methodology. **Panpan Li:** Supervision, Investigation, Formal analysis. **Bingxin Liu:** Supervision, Project administration, Investigation.

Declaration of competing interest

The authors declare that they have no known competing financial interests or personal relationships that could have appeared to influence the work reported in this paper.

Acknowledgments

This work is financially supported by National Natural Science Foundation of China No. 52265027; Natural Science Foundation of Qinghai province (No. 2024-ZJ-794).

Appendix A. Supplementary data

Supplementary data to this article can be found online at https://doi.org/10.1016/j.apsusc.2025.164471.

Data availability

Data will be made available on request.

References

[1] S. Li, Q. Li, R.W. Carpick, P. Gumbsch, X.Z. Liu, X. Ding, J. Sun, J. Li, The evolving quality of frictional contact with graphene, Nature 539 (2016) 541–545.

[2] L. Liu, M. Zhou, L. Jin, L. Li, Y. Mo, G. Su, X. Li, H. Zhu, Y. Tian, Recent advances in friction and lubrication of graphene and other 2D materials: mechanisms and applications, Friction 7 (2019) 199–216.

[3] J. Li, T. Gao, J. Luo, Superlubricity of graphite induced by multiple transferred graphene nanoflakes, Adv. Sci. 5 (2018) 1700616.

[4] D. Berman, S.A. Deshmukh, S.K.R.S. Sankaranarayanan, A. Erdemir, A.V. Sumant, Macroscale superlubricity enabled by graphene nanoscroll formation, Science 348 (2015) 1118–1122.

[5] P. Li, P. Ju, L. Ji, H. Li, X. Liu, L. Chen, H. Zhou, J. Chen, Toward robust macroscale superlubricity on engineering steel substrate, Adv. Mater. 32 (2020) 2002039.

[6] R. Li, X. Yang, M. Ma, J. Zhang, Hydrogen-enhanced catalytic conversion of amorphous carbon to graphene for achieving superlubricity, Small 19 (2023) 2206580.

[7] M. Urbakh, Friction: towards macroscale superlubricity, Nat. Nanotechnol. 8 (2013) 893–894.

[8] W. Cheng, W. Zhang, J. Tao, F. Zheng, B. Chu, R. Wang, C. Fang, L. Huai, P. Tao, C. Song, W. Shang, B. Fu, T. Deng, Octopus-like microstructure of graphene oxide generated through laser–microdroplet interaction for adhesive coating, ACS Nano 18 (2024) 7877–7889.

[9] Y. Sun, Y. Wang, E. Wang, B. Wang, H. Zhao, Y. Zeng, Q. Zhang, Y. Wu, L. Gu, X. Li, K. Liu, Determining the interlayer shearing in twisted bilayer MoS2 by nanoindentation, Nat. Commun. 13 (2022) 3898.

[10] T. Mindivanferda*Bilecik, Effect of various initial concentrations of CTAB on the noncovalent modified graphene oxide (MGNO) structure and thermal stability, Mater. Test. 59 (2017) 729–734.

[11] F. Mindivan, M. Gkta, Preparation of new PVC composite using green reduced graphene oxide and its effects in thermal and mechanical properties, Polym. Bull. 77 (2020) 1929–1949.

[12] F. Mindivan, M. Gkta, Effects of various vitamin C amounts on the green synthesis of reduced graphene oxide, Mater TEST 61 (2019) 1007–1011.

[13] F. Mindivan, M. Gkta, Rosehip-extract-assisted green synthesis and characterization of reduced graphene oxide, Chemistry Select 29 (2020) 8980–8985.

[14] X. Ge, J. Li, H. Wang, C. Zhang, J. Luo, Macroscale superlubricity under extreme pressure enabled by the combination of graphene-oxide nanosheets with ionic liquid, Carbon 151 (2019) 76–83.

[15] D. Berman, A. Erdemir, A.V. Sumant, Graphene: a new emerging lubricant, Mater. Today 17 (2014) 31–42.

[16] R. Yuan, P. Li, L. Chen, J. Yuan, J. Chen, Effects of grafting oxygen atoms on the tribological properties of graphene: molecular dynamics simulation and experimental analysis, Appl. Surf. Sci. 528 (2020) 147045.

[17] F.C. Mindivan, Alime, Tribo-material based on a UHMWPE/RGOC biocomposite for using in artificial joints, J. Appl. Polym. Sci. 31 (2021) 50768.

[18] J.E. Andrews, Y. Wang, S. Sinha, P.W. Chung, S. Das, Roughness-induced chemical heterogeneity leads to large hydrophobicity in wetting-translucent nanostructures, J. Phys. Chem. C 18 (2017) 10010–10017.

[19] N.M. Florea, et al., Novel nanocomposites based on epoxy resin/epoxy-functionalized polydimethylsiloxane reinforced with POSS, Composites Part B 75 (2015) 226–234.

[20] J. Chen, X. Chen, Z. Hao, Z. Wu, M.S. Selim, J. Yu, Y. Huang, Robust and superhydrophobic polydimethylsiloxane/Ni@Ti3C2Tx nanocomposite coatings with assembled eyelash-like microstructure array: a new approach for effective passive anti-icing and active photothermal deicing, ACS Appl. Mater. Interfaces 16 (2024) 20.

[21] M.S. Selim, S.A. El-Safty, M.A. Shenashen, A. Elmarakbi, Advances in polymer/inorganic nanocomposite fabrics for lightweight and high-strength armor and ballistic-proof materials, Chem. Eng. J. 493 (2024) 44.

[22] M.S. Selim, N.A. Fatthallah, S.A. Higazy, W. Zhuorui, Z. Hao, Superhydrophobic silicone/graphene oxide-silver-titania nanocomposites as eco-friendly and durable maritime antifouling coatings, Ceram. Int., 50 (1) 452-463.

[23] Y. Zou, Z. Chen, Z. Peng, C. Yu, W. Zhong, Mechanically strong multifunctional three-dimensional crosslinked aramid nanofiber/reduced holey graphene oxide and aramid nanofiber/reduced holey graphene oxide/polyaniline hydrogels and derived films, Nanoscale 39 (2021) 16734–16747.

[24] D.B. Cordes, P.D. Lickiss, F. Rataboul, Recent developments in the chemistry of cubic polyhedral oligosilsesquioxanes, Chem. Rev. 110 (2010) 2081–2173.

[25] Y. Shao, D. Han, Y. Tao, F. Feng, G. Han, B. Hou, H. Liu, S. Yang, Q. Fu, W. B. Zhang, Leveraging macromolecular isomerism for phase complexity in janus nanograins, ACS Cent. Sci. 9 (2023) 289–299.

[26] N. Divakaran, M.B. Kale, T. Senthil, S. Mubarak, D. Dhamodharan, L. Wu, J. Wang, Novel unsaturated polyester nanocomposites via hybrid 3D POSS-modified graphene oxide reinforcement: electro-technical application perspective, Nanomater 10 (2020) 260.

[27] W.-H. Liao, S.-Y. Yang, S.-T. Hsiao, Y.-S. Wang, S.-M. Li, C.-C.-M. Ma, H.-W. Tien, S.-J. Zeng, Effect of octa(aminophenyl) polyhedral oligomeric silsesquioxane functionalized graphene oxide on the mechanical and dielectric properties of polyimide composites, ACS Appl. Mater. Interfaces 6 (2014) 15802–15812.

[28] L. Sun, M. Cao, F. Xiao, J. Xu, Y. Chen, POSS functionalized graphene oxide nanosheets with multiple reaction sites improve the friction and wear properties of polyamide 6, Tribol. Int. 154 (2021) 106747.

[29] B. Yu, K. Wang, Y. Hu, F. Nan, J. Pu, H. Zhao, P. Ju, Tribological properties of synthetic base oil containing polyhedral oligomeric silsesquioxane grafted graphene oxide, RSC Adv. 8 (2018) 23606–23614.

[30] R. Yuan, L. Ji, Y. Wu, H. Li, P. Ju, L. Chen, H. Zhou, J. Chen, "Plate-anchor" shaped POSS-functionalized graphene oxide with self-fixing effect in polyimide matrix: Molecular dynamic simulations and experimental analysis, Comp. Sci. Technol. 176 (2019) 103–110.

[31] atomic steps, Sci. Adv., 5 (2019) 0513.

[32] P. Serles, T. Arif, A.B. Puthirath, S. Yadav, G. Wang, T. Cui, A.P. Balan, T.P. Yadav, P. Thibeorchews, N. Chakingal, Friction of magnetene, a non–van der Waals 2D material, Sci. Adv. 7 (2021) 2041.

[33] R. Garcia, Interfacial liquid water on graphite, graphene, and 2D materials, ACS Nano 17 (2022) 51–69.

[34] Z. Xu, Y. Zhao, Y. Yan, H. Zhang, Corrosion properties of sodium carboxymethyl cellulose on metal surface base on molecular dynamics simulation, Comput. Mater. Sci 228 (2023) 112295.

[35] G. Tang, Z. Wu, F. Su, H. Wang, X. Xu, Q. Li, G. Ma, P.K. Chu, Macroscale superlubricity on engineering steel in the presence of black phosphorus, Nano Lett. 21 (2021) 5308–5315.

[36] B. Luan, R. Zhou, Spontaneous transport of single-stranded DNA through graphene–MoS2 heterostructure nanopores, ACS Nano 12 (2018) 3886–3891.

[37] H. Zhao, D. Bahamon, M. Khaleel, L.F. Vega, Insights into the performance of hybrid graphene oxide/MOFs for CO2 capture at process conditions by molecular simulations, Chem. Eng. J. 449 (2022) 137884.

[38] Y. Pang, J. Yang, T.E. Curtis, S. Luo, D. Huang, Z. Feng, J.O. Morales-Ferreiro, P. Sapkota, F. Lei, J. Zhang, Exfoliated graphene leads to exceptional mechanical properties of polymer composite films, ACS Nano 13 (2019) 1097–1106.

[39] R. Yuan, L. Gao, J. Liu, C. Tu, R. Tan, S. Xu, Effect of hydrophobic alkyl chains on the plasticization properties of citrate: experiments and MD simulation, Eur. Polym. J. 203 (2024) 112644.

[40] D.T. Ho, H.S. Park, S.Y. Kim, U. Schwingenschlögl, Graphene origami with highly tunable coefficient of thermal expansion, ACS Nano 14 (2020) 8969–8974.

[41] H. Shen, X. Zou, H. Yang, W. Zhong, Y. Wang, S. Wang, M. Deng, Adsorption of organic molecules and surfactants on graphene: a coarse-grained study, J. Phys. Chem. A 125 (2021) 700–711.

[42] D. Wei, C. Zhao, A. Khan, L. Sun, Y. Ji, Y. Ai, X. Wang, Sorption mechanism and dynamic behavior of graphene oxide as an effective adsorbent for the removal of chlorophenol based environmental-hormones: a DFT and MD simulation study, Chem. Eng. J. 375 (2019) 121964.

[43] Y. Zhang, S. Wang, P. Tang, Z. Zhao, Z. Xu, Z.-Z. Yu, H.-B. Zhang, Realizing spontaneously regular stacking of pristine graphene oxide by a chemical-structure-engineering strategy for mechanically strong macroscopic films, ACS Nano 16 (2022) 8869–8880.

[44] H. Bai, G. Zou, H. Bao, S. Li, F. Ma, H. Gao, Deformation coupled moiré mapping of superlubricity in graphene, ACS Nano 17 (2023) 12594–12602.

[45] O.C. Compton, D.A. Dikin, K.W. Putz, L.C. Brinson, S.B.T. Nguyen, Electrically conductive 'alkylated' graphene paper via chemical reduction of amine-functionalized graphene oxide paper, Adv. Mater. 22 (2010) 892–896.

[46] B. Decker, C. Hartmann-Thompson, P.I. Carver, S.E. Keinath, P.R. Santurri, Multilayer sulfonated polyhedral oligosilsesquioxane (S-POSS)-sulfonated polyphenylsulfone (S-PPSU) composite proton exchange membranes, Chem. Mater. 22 (2009) 942–948.

[47] A. Kouloumpis, E. Thomou, N. Chalmpes, K. Dimos, K. Spyrou, A.B. Bourlinos, I. Koutselas, D. Gournis, P. Rudolf, Graphene/carbon dot hybrid thin films prepared by a modified langmuir–schaefer method, ACS Omega 2 (2017) 2090–2099.

[48] Y. Ma, H. Di, Z. Yu, L. Liang, L. Lv, Y. Pan, Y. Zhang, D. Yin, Fabrication of silica-decorated graphene oxide nanohybrids and the properties of composite epoxy coatings research, Appl. Surf. Sci. 360 (2016) 936–945.

[49] Y. Ye, D. Zhang, T. Liu, Z. Liu, W. Liu, J. Pu, H. Chen, H. Zhao, X. Li, Improvement of anticorrosion ability of epoxy matrix in simulate marine environment by filled with superhydrophobic POSS-GO nanosheets, J. Hazard. Mater. 364 (2019) 244–255.

[50] L. Frérot, A. Crespo, J.A. El-Awady, M.O. Robbins, J. Cayer-Barrioz, D. Mazuyer, From molecular to multiasperity contacts: how roughness bridges the friction scale gap, ACS Nano 17 (2023) 2205–2211.

[51] S. Wang, L. Li, Q. Zou, J. Chen, X. Zhao, Y. Xie, Y. Hu, K. Yang, Abrasion mechanisms of superhydrophobic coating surfaces wetted in Wenzel state, Colloids Surf. A 657 (2023) 130585.

[52] X. Gao, J. Zhang, P. Ju, J. Liu, L. Ji, X. Liu, T. Ma, L. Chen, H. Li, H. Zhou, Shear-induced interfacial structural conversion of graphene oxide to graphene at macroscale, Adv. Funct. Mater. 30 (2020) 2004498.

[53] M. Roksana, D. Sabina, P. Tadeusz, C. Maciej, G. Grayna, Characterization of graphite oxide and reduced graphene oxide obtained from different graphite precursors and oxidized by different methods using raman spectroscopy, Materials 11 (2018) 1050.